nature photonics

Article

https://doi.org/10.1038/s41566-024-01386-2

A conformal mapping approach to broadband nonlinear optics on chip

Received: 7 November 2022

Accepted: 8 January 2024

Published online: 12 February 2024

Check for updates

Chunyu Huang[1], Yu Luo[2,3] ✉, Yule Zhao[1], Xiaofei Ma[1], Zhiwei Yan[1], Ziyi Liu[1], Chong Sheng[1], Shining Zhu[1] & Hui Liu[1] ✉

Integrated nonlinear optical devices play an important role in modern optical communications; however, conventional on-chip optical devices with homogeneous or periodic translation dimensions generally have limited bandwidth when applied to nonlinear optical applications. So far there lacks a general method to design compact nonlinear optical devices capable of operating over a broadband continuous frequency range. In this work we propose a general strategy based on transformation optics to design curved accelerating waveguides with spatially gradient curvatures, which can achieve broadband nonlinear frequency conversion on chip. Through rigorous analytical calculation, we show that increasing the acceleration (that is, the gradient in the waveguide curvature) broadens the output signal spectrum in the nonlinear process. In this experiment we use sum-frequency generation for infrared signal upconversion as an example and fabricated a variety of curved accelerating waveguides using thin-film lithium niobate on insulators. Efficient sum-frequency generation is observed over a broadband continuous spectrum. Our conformal mapping approach offers a platform for various nonlinear optical processes and works in any frequency range, including visible, infrared and terahertz bands. Apart from lithium niobate on insulators, our approach is also compatible with other nonlinear materials such as silicon, silicon nitride and chalcogenide glasses and so on.

Broadband nonlinear optical structures have versatile applications in high-speed optical communication and computing[1–4], integrated quantum chips[5], long-wave photon detection[6], material spectral analysis[7], microwave photonics[8,9], broadband spectrum detection[10], molecular sensing and spectroscopy[11–13], and so on. The high demand for integrated optical applications[14], including transmitters, modulators[15,16], and wavelength division multiplexers[17], urgently calls for broadband nonlinear optical components on chip. To this end, various approaches have been proposed; for example, in the domain of third-order nonlinearities ($\chi^{(3)}$), group-velocity dispersion engineering has been applied to broadband four-wave mixing[18] and cascaded waveguides have enabled supercontinuum light generation[19,20]. Through group-velocity dispersion tuning, broadband nonlinear effects related to quadratic nonlinearities ($\chi^{(2)}$) have also been observed[21], and entangled photons were generated in periodically poled lithium niobate waveguides[22]. However, owing to the chromatic dispersion effect in nonlinear materials, these nonlinear processes generally have limited bandwidths. Although the frequency comb of an integrated optical microcavity offers a possible route to design multifrequency light sources[23,24], the output signal is not strictly continuous over a broadband spectrum.

In this work we deploy conformal transformation optics (CTO) to break the conservation law of photon momentum and in turn obtain

[1]Collaborative Innovation Center of Advanced Microstructures National Laboratory of Solid State Microstructures, School of Physics Nanjing University, Nanjing, China. [2]School of Electrical and Electronic Engineering, Nanyang Technological University, Singapore, Singapore. [3]Key Laboratory of Radar Imaging and Microwave Photonics, Nanjing University of Aeronautics and Astronautics, Nanjing, China. ✉e-mail: yu.luo@nuaa.edu.cn; liuhui@nju.edu.cn

broadband nonlinear optical responses over a continuous spectrum. This approach is highly suitable for designing translational/rotational symmetry-broken structures, whose nonlinear responses are difficult to investigate via a conventional approach[18,21,22]. Moreover, this approach is not necessarily limited to $\chi^{(2)}$ or $\chi^{(3)}$, and is applicable to a general class of nonlinear processes. Last but not least, our experimental realizations also extend the domain of transformation optics (TO) from linear to nonlinear optics; TO relates a novel optical phenomenon (which is in general difficult to achieve with traditional optical methods) to the material parameters required for its occurrence[25,26]. It provides additional degrees of freedom to manipulate electromagnetic waves through properly engineering the permittivity and permeability across space and time[27,28]. Transformation optics has found various novel applications in, for example, cloaking[29–35], illusion optics[36] and mimicking cosmic phenomena[37–42]. However, as materials obtained from TO are often strongly inhomogeneous and extremely anisotropic, these applications are generally difficult to realize experimentally, especially at high frequencies (for example, the infrared, visible and beyond). Conformal and quasiconformal mappings solve this problem by eliminating extreme anisotropy[26,43–45], pushing TO technology one step closer towards real-world applications. Apart from the devices mentioned above, constant curved microstuctures[46–48], broadband light harvesters[49], Luneburg lenses[50] and Maxwell's fish-eye lenses[51] have also been designed and implemented under the CTO framework. In all relevant experimental realizations, CTO is applied mainly to linear material parameters. In this work we go one step beyond and show that CTO offers great potential to extend the bandwidth of nonlinear optical devices. More specifically, a general conformal mapping approach is developed to transform a curved accelerating waveguide (CAW) with a gradient radius of curvature into a straight waveguide with a spatially inhomogeneous refractive index and nonlinear susceptibility. Through transformed wave-equation and effective nonlinear coefficients, we construct the nonlinear couple-wave equations (CWEs) of CAWs. Nobly, the bandwidth of the nonlinear frequency conversion can be effectively controlled by the acceleration parameter, that is, the gradient of the waveguide curvature. The greater the acceleration, the broader the bandwidth of the output signal. As experimental proof, we take the sum-frequency generation for infrared signal upconversion (SFG-ISU) as the example, fabricate CAWs on lithium niobate on insulators (LNOIs), and demonstrate that the SFG-ISU bandwidth can be efficiently broaden over an ultra-broad frequency range (that is, four-times broader than a straight optical waveguide designed with the traditional phase-matching approach). We highlight that the broadband SFG-ISU demonstrated here is just one specific application. Our method can be easily extended to other nonlinear processes and is compatible with other nonlinear materials. Moreover, CAW structures experimentally realized here are easy to integrate on chip, robust to temperature and compatible with the complementary metal–oxide semiconductor (CMOS) process.

Results

The CTO approach to designing CAWs

Our on-chip broadband nonlinear processes make use of CTO to design CAWs (Fig. 1a) that are uniform in width but gradient in bending curvature. The cross-section is detailed in the bottom-right inset of Fig. 1a, whereas bandwidth broadening is illustrated in the upper-right inset. Such a waveguide has a width of 1 μm, a total length of 60 μm, and is etched into a 370-nm-thick z-cut LNOI substrate. As we employed a rectangular waveguide, the conformal mapping in each (x, y) plane is the same ($z = w$). We therefore aim to find a general two-dimensional conformal mapping $\xi = f(\zeta)$ that transforms a curved waveguide in the physical space $\xi = x + iy$ to a straight waveguide in the virtual space $\zeta = u + iv$. The former has a spatially gradient radius $r(v)$ as an arbitrary function of v. The conformal mapping $f(\zeta)$ under a given $r(v)$ ensures that the total length of the waveguide remains unchanged under the transformation, that is, $|d\xi| = r(v)d\theta = dv$, where $\theta(v) = \int_0^v dv'/r(v')$ denotes the angle between the tangential direction of the curved waveguide and the vertical axis of the physical coordinate. The conformal mapping is then obtained through the integration of $\theta(-i\zeta')$ in terms of $\xi = \int_0^{-i\zeta} e^{i\theta(-i\zeta')} d\zeta'$ (see Supplementary Section 1.1 for detailed derivations). The theory of CTO enables us to calculate the refractive index of the straight waveguide

$$n = n_\xi \left|\frac{d\xi}{d\zeta}\right| = n_\xi \left|e^{i\theta(-i\zeta)}\right| \tag{1}$$

which is directly related to $\theta(-i\zeta)$, where n_ξ is the refractive index of the material in the real space. When the radius is a constant, r_0, $\theta(-i\zeta) = -i\zeta/r_0$ and the refractive index of the straight waveguide takes an exponential form $n = n_0 e^{u/r_0}$, in agreement with a previous study on uniformly curved waveguides[46] (Supplementary Information). To design the CAW, we consider a spatially gradient radius of curvature given by

$$r(v) = \frac{r_0'}{\ln\left(n_0'\sqrt{1 - av} - n_1'\right)} \tag{2}$$

where $r_0' = 25.56$ μm, $n_0' = 1,847.7$ and $n_1' = 1,849.2$ are constants to be determined through initial conditions, and a is the acceleration parameter to characterize different CAWs (see the Supplementary Information for transformations of two more curved waveguides to illustrate the generality).

Using the conformal mapping approach described above, the CAW in Fig. 1a is transformed into a straight waveguide with a spatially gradient refractive index, as depicted in Fig. 1b. The two-dimensional index distribution in the (u, v)-plane is depicted in the inset of Fig. 1b. The indexes of lithium niobate in the physical space are obtained from ref. 52. To demonstrate the continuous variation of the refractive index along both u and v, we plot $n(u, v)$ as a function of v (u) at several different u (v) in Fig. 1c (Fig. 1d). Figure 1c illustrates that $n(u, v)$ has different monotonicity for $u = -0.25, 0, 0.25$ μm. Figure 1d illustrates the greater variation across the index values with increasing v.

We are interested in the eigenmode propagating along the v direction, for which we need to consider the the effective mode index defined as $n_{\text{eff}} = k_v/k_0$, where k_v represents the propagating constant and k_0 denotes the free-space wavevector; k_v can be obtained through simulation of the mode field distribution at a fixed v. Due to the spatially inhomogeneous refractive index distribution in the transformed space, n_{eff} varies along v. Detailed calculations show that, for a radius given by equation (2), the mode index can be written as a simple function of v, that is

$$n_{\text{eff}}(v, \omega) = n_{\text{eff}}(0, \omega)\sqrt{1 - a(\omega)v} \tag{3}$$

where we have introduced the frequency dependent acceleration $a(\omega)$. A larger acceleration clearly corresponds to a larger gradient in the effective mode index, which in turn compensates for the phase mismatches at different frequencies, giving rise to the broadband nonlinear wave-mixing process.

As the radius decreases in a CAW, the mode field distribution tends to become distorted and accumulates energy towards the right side of the waveguide, as demonstrated by the two insets in Fig. 1d. This is due to the fact that the transformed refractive index n exhibits an increasing trend with u. The distorted field distribution has two effects: first, it tends to decrease the effective mode area of the CAW, thereby enhancing the intensity of the electric field involved in the nonlinear interaction (a smaller effective mode area induces a larger electric field intensity in the waveguide; see Supplementary Section 3) as $r(v)$ decreases (see the red line plotted in Supplementary Fig. 2); second, it increases the mode overlap between the fundamental and higher-order modes due to the

https://doi.org/10.1038/s41566-024-01386-2

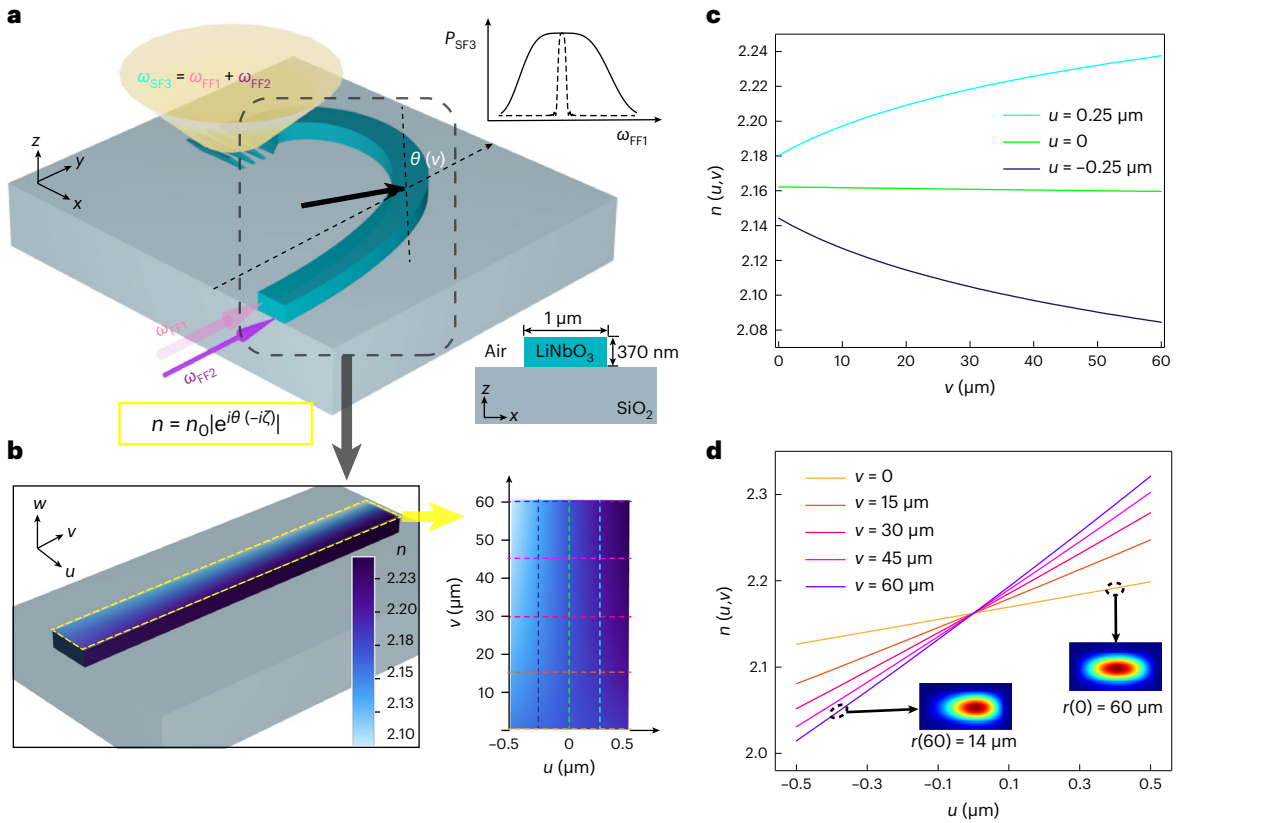

Fig. 1 | Schematic of the CAW for broadband SFG-ISU. a, The CAW with the spatially gradient radius $r(v)$ in the physical space (x, y, z), where $r(v)$ is given by equation (2). The cross-section of the waveguide and a schematic diagram of the extended bandwidth are depicted in the bottom- and top-right insets, respectively. **b**, The refractive index distribution of the transformed straight waveguide in the virtual space (u, v, w). A two-dimensional index map (with respect to u and v) of the top surface of the waveguide (highlighted by the yellow box) is shown to the right. **c**. Refractive index distributions at $u = -0.25, 0, 0.25$ μm (see the three vertical dashed lines in **b**). **d**. Refractive index distributions at $v = 0, 15, 30, 45, 60$ μm (see the five horizontal dashed lines in **b**). The two insets plot the eigenmode distributions of the CAW at different v ($v = 0$ and $v = 60$ μm). The corresponding radii are $r(0) = 60$ μm and $r(60\ \mu m) = 14$ μm.

asymmetric mode field distribution with respect to $u = 0$ (demonstrated in Supplementary Section 1.3). Both effects contribute to the enhancement of the effective nonlinear coefficients, as shown by the blue line in Supplementary Fig. 2.

Broadband nonlinear up-conversion by CAWs

In this section we demonstrate that the above-designed CAW provides an effective means to broaden the nonlinear process. For the effective mode index given by equation (3), the wave equation governing the electric field in the CAW is given by,

$$\nabla^2 E - \frac{n_{\text{eff}}^2(0,\omega)(1-av)}{c^2}\frac{\partial^2 E}{\partial t^2} = 0 \tag{4}$$

The propagation solution of equation (4) takes the form of,

$$E = \text{Ai}\left[\left(\frac{n_{\text{eff}}(0,\omega)k_0}{2a}\right)^{3/2}(av-1)\right] + i\text{Bi}\left[\left(\frac{n_{\text{eff}}(0,\omega)k_0}{2a}\right)^{3/2}(av-1)\right] \tag{5}$$

where $\text{Ai}(\cdot)$ and $\text{Bi}(\cdot)$ are Airy functions of the first and the second kind, respectively. As we are interested in the case in which the refractive index $n_{\text{eff}}(v, \omega)$ varies slowly along v, such a solution can be approximated to $E \approx (1-av)^{-1/4}\exp[i\phi(v,\omega)]$, where the phase $\phi(v, \omega)$ of the transformed electric field in the CAW is a quadratic function of v, that is, $\phi(v,\omega) = n_{\text{eff}}(0,\omega)k_0(v - av^2/4)$.

The eigenfunctions of the electric fields and effective nonlinear coefficients d_{eff} enable us to couple the fundamental and harmonic waves through the nonlinear CWEs (see Supplementary Equation (11)). In the traditional SFG process, the phase mismatch $\Delta\phi$ between the fundamental and sum-frequency is a constant. As a result, efficient SFG can only be achieved at a specific frequency when the phase mismatch is strictly zero, that is, $\Delta\phi = 0$. By contrast, in our CAWs, the spatially gradient $\Delta\phi(v, \omega)$ suppresses the phase mismatch at different frequencies, giving rise to an efficient nonlinear conversion over a broadband continuous frequency range. A larger acceleration corresponds to a larger gradient in $\Delta\phi$, and hence a broader bandwidth of the frequency conversion. Moreover, the transformed eigenmode fields of the fundamental and harmonic frequencies tend to enhance their nonlinear coupling coefficients d_{eff} in CAWs (see Supplementary Equation (12)), which further increases the nonlinear conversion efficiency.

To demonstrate the broadband nonlinear response, we compare the nonlinear frequency conversion efficiencies and bandwidths of a uniformly curved waveguide (characterized by $a = 0$), and 11 CAWs with gradually increased accelerations (that is, $a = 1.88$, $5.34, \ldots, 73.43\text{m}^{-1}$). As shown in Fig. 2a, a larger acceleration corresponds to a larger gradient of curvature. Consequently, the mode index n_{eff} (and hence the phase mismatch $\Delta\phi$) and the effective nonlinear coefficient d_{eff} changes more rapidly along v, as depicted in Fig. 2b. As mentioned before, the rapid variation in $\Delta\phi$ suppresses the phase mismatch, leading to an efficient nonlinear conversion over a broadband frequency range. The results in Fig. 2c reveal that the SFG process

https://doi.org/10.1038/s41566-024-01386-2

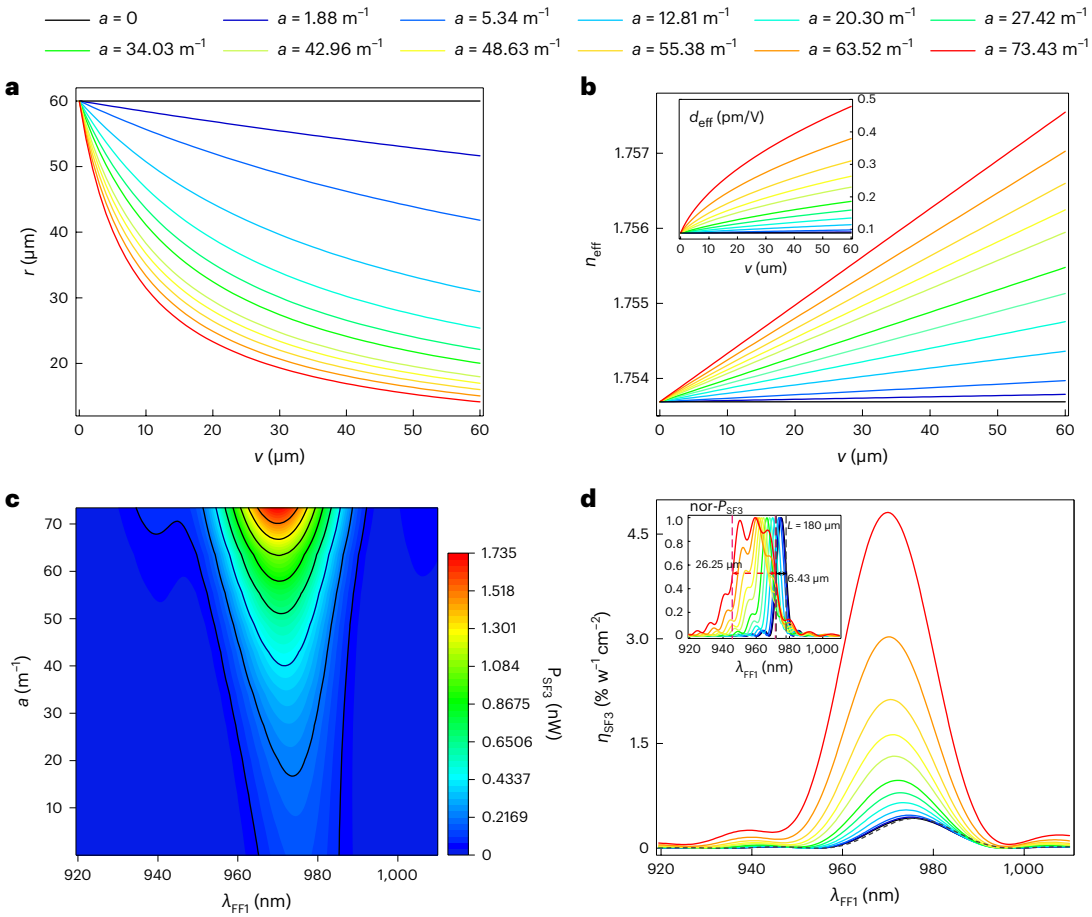

Fig. 2 | Theoretical analysis of the SFG-ISU mechanism in CAWs. a, Radii of 11 CAWs as a function of the vertical coordinate v. Larger acceleration corresponds to larger gradient in $r(v)$. The legends above the figure give the exact values of the accelerations of the 11 CAWs. **b**, The effective mode index distribution n_{eff} at the fundamental wavelength $\lambda_{\mathrm{FF2}} = 1,064$ nm for the 11 CAWs. The inset depicts the effective nonlinear coefficient $\widetilde{d}_{\mathrm{eff}}$ (the unit of effective nonlinear coefficient is pm/V; see Supplementary Section 1.3 for details) at $\lambda_{\mathrm{FF1}} = 960$ nm as a function of v. **c**, The contour plot of output sum-frequency power in terms of the fundamental wavelength λ_{FF1} and the acceleration a. **d**, The normalized frequency conversion efficiency $\eta_{\mathrm{SF3}} = P_{\mathrm{SF3}}/(P_{\mathrm{FF1}}P_{\mathrm{FF2}}L^2)$ as a function of the fundamental wavelength λ_{FF1}, where P_{SF3}, P_{FF2} and P_{FF1} denote the power of sum-frequency three and fundamental frequency one and two, while L represents the total length of the waveguide. The black dashed curve corresponds to the straight waveguide with homogeneous refractive index. The inset demonstrates that the normalized bandwidth of the CAW at $a = 73.43\ \mathrm{m}^{-1}$ can be four-times wider than that at $a = 0$ when the waveguide length is fixed at 180 μm, where nor-P_{SF3} is the power of sum-frequency three that is normalized by the maximum.

is considerably broadened and enhanced as a increases. Simultaneously, a larger effective nonlinear coefficient results in substantial enhancement of the SFG efficiency. This point is confirmed by Fig. 2d, which shows that the peak SFG efficiency increases from $0.4314\%\ \mathrm{W}^{-1}\mathrm{cm}^{-2}$ to $4.8155\%\ \mathrm{W}^{-1}\mathrm{cm}^{-2}$ (corresponding to a ten-fold enhancement) when a is changed from 0 to $73.43\ \mathrm{m}^{-1}$. For comparison, we also plot the SFG efficiency of a straight waveguide, as given by the black dashed line in Fig. 2d. Its bandwidth is considerably narrower and peak value is much smaller than those of CAWs. Besides, we highlight that the bandwidth of the nonlinear conversion can be further extended by increasing length of the CAW (the limitation of bandwidth increasing with acceleration is discussed in detail in the Supplementary Information). The inset of Fig. 2d illustrates that a CAW can enhance the SFG bandwidth by more than fourfold compared with a uniform waveguide fixed at 180 μm.

Before we proceed to the experimental realization, we pause to highlight the importance of CTO in our proposal. An optical structure with breaking translational/rotational symmetry generally does not have a well-defined wave vector. Consequently, the phase-matching condition is difficult to obtain, and with conventional approaches, one cannot tell which parameter plays an essential role in achieving broadband nonlinear effects. This problem becomes even more critical for 3D structures, for which the nonlinear numerical simulations are extremely time-consuming. The proposed CTO approach solves this problem, and its importance lies in the fact that: (1) it shows how the effective acceleration should be properly designed to broaden the nonlinear optical responses; and (2) it reveals the hidden symmetry in the symmetry-broken structure, enabling us to obtain the coupled-mode equations to simplify the nonlinear calculations/simulations. The CTO is therefore not only a means of analysing curved waveguides, but a general approach to guide the designs of a variety of nonlinear experiments with desired bandwidths.

Experimental proof for broadband nonlinear up-conversion

To investigate the broadband SFG-ISU experimentally, we fabricate the designed CAWs on a LNOI chip and detect the sum-frequency efficiency at different frequencies using a combination of both scientific CMOS (sCMOS) camera and spectrometer measurements. Our experimental set-up is shown in Fig. 3a and described in detail in the Methods. Two fundamental frequencies are a femtosecond laser to tune the frequency over a continuous spectrum ($\lambda_{\mathrm{FF1}} \in [920\ \mathrm{nm}, 1,010\ \mathrm{nm}]$) , and a continuous-wave laser fixed at $\lambda_{\mathrm{FF2}} = 1,064$ nm. The sample is pumped by TE_0 and TM_0 modes via a half-wave plate. The output light is filtered and then guided into the

https://doi.org/10.1038/s41566-024-01386-2

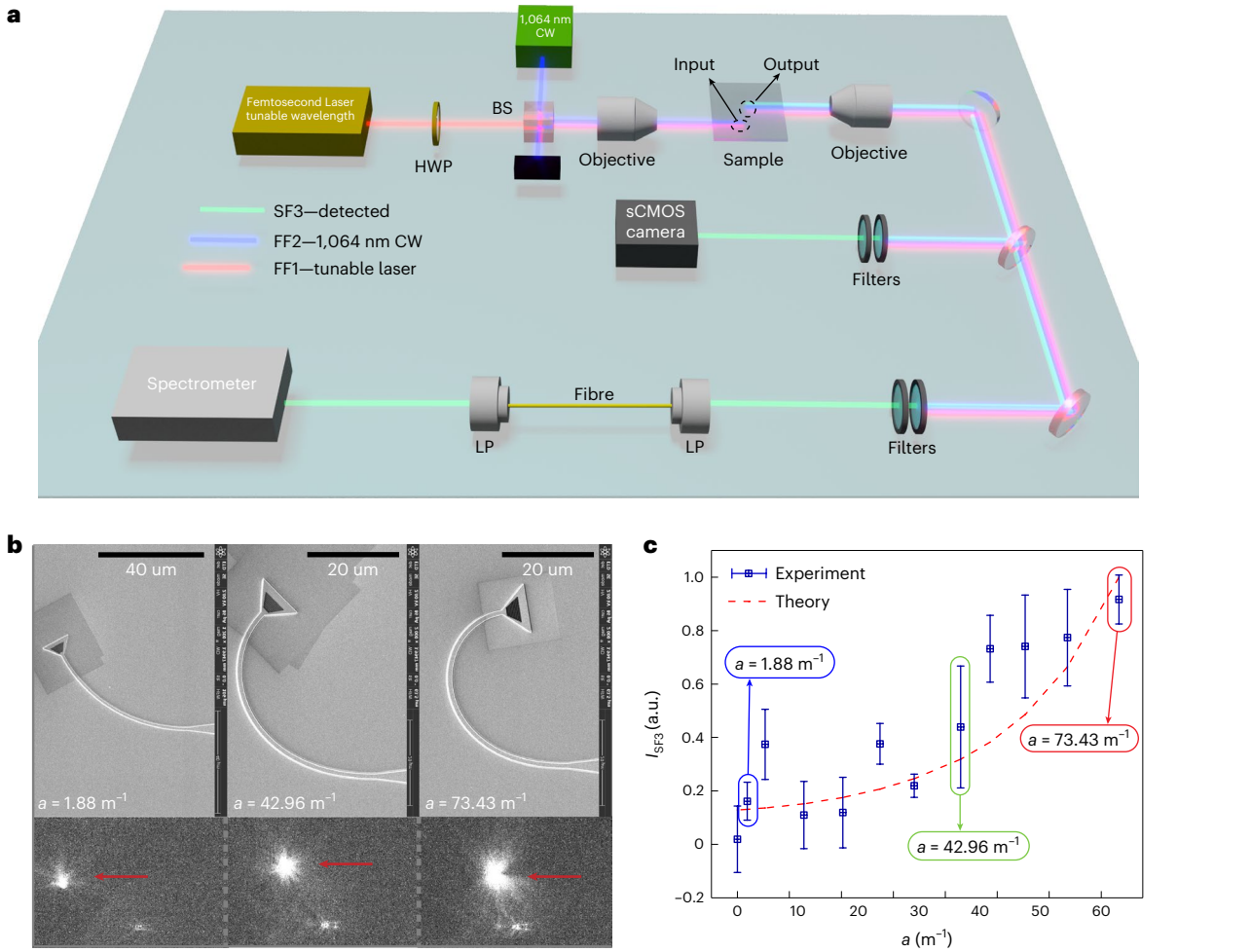

Fig. 3 | Experimental demonstration of enhanced SFG-ISU. a, Schematic of the experimental set-up. **b**, The three pictures at the bottom show the SFG of CAWs taken by the sCMOS camera, where the red arrows indicate the SFG output points of the CAWs. The three pictures at the top are the corresponding scanning electron microscopy images of CAWs fabricated by a focused ion beam (FIB). **c**, The measured SFG output intensity as a function of the acceleration a (at $\lambda_{FF1} = 960$ nm). The error bars indicate the s.d. a.u., arbitrary units.

sCMOS camera (spectrometer) in the middle (bottom) channel for measurement.

We first investigate the SFG enhancement of CAWs at the fixed wavelength $\lambda_{FF1} = 960$ nm, which can be directly reflected by images captured by the camera. We judiciously adjust the measurement set-up to keep the input condition unchanged for different samples and then combine the images of output SFG signals from eleven different CAWs into a GIF for comparison (Supplementary Information). Figure 3b displays three out of the eleven images at $a = 1.88\ \mathrm{m}^{-1}, 42.96\ \mathrm{m}^{-1}$ and $73.43\ \mathrm{m}^{-1}$. Apparently, CAWs with larger accelerations give rise to a brighter and spatially wider output spot. The average from multiple measurements of the eleven CAWs confirms that the SFG efficiency increases with acceleration (as shown in Fig. 3c), in excellent agreement with our theoretical prediction. This result was also verified by a spectrometer; one of the tests is shown in Fig. 4a.

To more quantitatively analyse the SFG bandwidth broadening, we scan λ_{FF1} continuously from 920 nm to 1,010 nm. Note that both the sCMOS camera (Fig. 3b) and spectrometer (Fig. 4a) alone can detect the efficiency of the frequency conversion at a fixed wavelength[52–54]. However, neither of them can be applied to the detection of broadband SFG because the transmission of the system is strongly frequency dependent (that is, the nonlinear conversion efficiency is no longer equivalent to the signal intensity captured by the sCMOS camera or the spectrometer). To solve this problem, we introduce a fibre-lens system to quantify the transmission of the system through the second-harmonic generation measured by our combined sCMOS camera/spectrometer system (see Supplementary Section 2.2 for details). The broadband SFG efficiency is then obtained by normalizing the results obtained by the spectrometer with respect to the transmission spectrum. As shown in Fig. 4b, the SFG spectra obtained in this way agrees quite well with the theoretically predicted ones. More interestingly, the full-width at half-maximum plotted in Fig. 4c reveals that the SFG bandwidth increases dramatically with acceleration.

Discussion

We have demonstrated a novel physical mechanism to achieve broadband nonlinear optical process through the introducing of CTO. We especially designed and fabricated a type of CAW to demonstrate the effectiveness of this mechanism experimentally. Our experiments yielded efficient SFG-ISU with a broadband spectrum. Notably, by adjusting the structure parameters of the waveguide, we can tune the bandwidth of the output SFG-ISU. Our results show that the bandwidth of SFG-ISU increases with the acceleration parameter, with no sacrifice of efficiency for a compressed mode field.

This work demonstrates the feasibility of broadband nonlinear devices by near-infrared up-conversion detection, which could be extended to any other wavelength band. Our method not only overcomes the limitation of materials but also provides flexible and

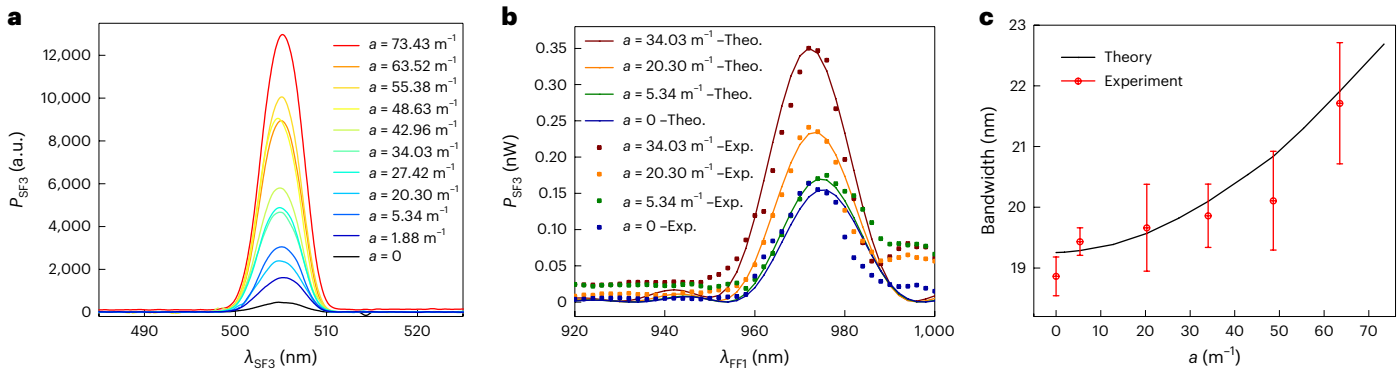

Fig. 4 | Experimental demonstration of broadband SFG in CAWs with different accelerations. a, One-time tested spectrum with λ_{FF1} = 960 nm. The spectra are smoothened. a.u., arbitrary units. **b**, Sum-frequency generation intensities of different CAWs as a function of the scanned wavelength λ_{FF1}. **c**, Sum-frequency generation bandwidths for CAWs with different accelerations. The error bars indicate the s.d.

expansible applications to many other nonlinear optical processes in integrated systems, including differential frequency generation, four-wave mixing, parametric down-conversion and so on. Moreover, the broadband nonlinear process is achieved by controlling the waveguide's geometrical shape, and the fabrication process is straightforward, which makes our strategy suitable for large-scale industrial production. In the future, our method has great potential in integrated nonlinear photonics and various related optical applications.

Online content

Any methods, additional references, Nature Portfolio reporting summaries, source data, extended data, supplementary information, acknowledgements, peer review information; details of author contributions and competing interests; and statements of data and code availability are available at https://doi.org/10.1038/s41566-024-01386-2.

References

1. Smith, S. D. Lasers, nonlinear optics and optical computers. *Nature* **316**, 319–324 (1985).
2. Arumugam, M. Optical fiber communication—an overview. *Pramana* **57**, 849–869 (2001).
3. *Encyclopedia of Modern Optics* (eds Guenther, B. D. & Steel, D.) 69–77 (Elsevier, 2005).
4. Boyd, R.W. in *Nonlinear Optics* 3rd edn, Ch. 7, 329–390 (Academic, 2008).
5. Wang, J., Sciarrino, F., Laing, A. & Thompson, M. G. Integrated photonic quantum technologies. *Nat. Photon.* **14**, 273–284 (2020).
6. Talghader, J. J., Gawarikar, A. S. & Shea, R. P. Spectral selectivity in infrared thermal detection. *Light: Sci. Appl.* **1**, e24 (2012).
7. Prylepa, A. et al. Material characterisation with methods of nonlinear optics. *J. Phys. D* **51**, 043001 (2018).
8. Capmany, J. & Novak, D. Microwave photonics combines two worlds. *Nat. Photon.* **1**, 319–330 (2007).
9. Marpaung, D., Yao, J. & Capmany, J. Integrated microwave photonics. *Nat. Photon.* **13**, 80–90 (2019).
10. Xomalis, A. et al. Detecting mid-infrared light by molecular frequency upconversion in dual-wavelength nanoantennas. *Science* **374**, 1268–1271 (2021).
11. Kalashnikov, D. A., Paterova, A. V., Kulik, S. P. & Krivitsky, L. A. Infrared spectroscopy with visible light. *Nat. Photon.* **10**, 98–101 (2016).
12. De Bruyne, S., Speeckaert, M. M. & Delanghe, J. R. Applications of mid-infrared spectroscopy in the clinical laboratory setting. *Crit. Rev. Clin. Lab. Sci.* **55**, 1–20 (2018).
13. Huang, K., Fang, J., Yan, M., Wu, E. & Zeng, H. Wide-field mid-infrared single-photon upconversion imaging. *Nat. Commun.* **13**, 1077 (2022).
14. Ready JF. in *Industrial Applications of Lasers* 2nd edn, Ch. 23, 546–558 (Academic, 1997).
15. Wang, C. et al. Integrated lithium niobate electro-optic modulators operating at CMOS-compatible voltages. *Nature* **562**, 101–104 (2018).
16. He, M. et al. High-performance hybrid silicon and lithium niobate Mach–Zehnder modulators for 100 Gbit s^{-1} and beyond. *Nat. Photon.* **13**, 359–364 (2019).
17. Ishio, H., Minowa, J. & Nosu, K. Review and status of wavelength-division-multiplexing technology and its application. *J. Lightwave Technol.* **2**, 448–463 (1984).
18. Foster, M. A. et al. Broad-band optical parametric gain on a silicon photonic chip. *Nature* **441**, 960–963 (2006).
19. Singh, N. et al. Supercontinuum generation in varying dispersion and birefringent silicon waveguide. *Opt. Express* **27**, 31698–31712 (2019).
20. Wei, J. et al. Supercontinuum generation assisted by wave trapping in dispersion-managed integrated silicon waveguides. *Phys. Rev. Appl.* **14**, 054045 (2020).
21. Jankowski, M. et al. Ultrabroadband nonlinear optics in nanophotonic periodically poled lithium niobate waveguides. *Optica* **7**, 40–46 (2020).
22. Javid, U. A. et al. Ultrabroadband entangled photons on a nanophotonic chip. *Phys. Rev. Lett.* **127**, 183601 (2021).
23. Chang, L., Liu, S. & Bowers, J. E. Integrated optical frequency comb technologies. *Nat. Photon.***16**, 95–108 (2022).
24. Hu, Y, et al. High-efficiency and broadband on-chip electro-optic frequency comb generators. *Nat. Photon.* **16**, 679–685 (2022).
25. Pendry, J. B., Schurig, D. & Smith, D. R. Controlling electromagnetic fields. *Science* **312**, 1780–1782 (2006).
26. Leonhardt, U. Optical conformal mapping. *Science* **312**, 1777–1780 (2006).
27. McCall, M. W., Favaro, A., Kinsler, P. & Boardman, A. A spacetime cloak, or a history editor. *J. Opt.* **13**, 024003 (2010).
28. Horsley, S. A. R. Transformation optics, isotropic chiral media and non-Riemannian geometry. *New J. Phys.* **13**, 053053 (2011).
29. Cai, W., Chettiar, U. K., Kildishev, A. V. & Shalaev, V. M. Optical cloaking with metamaterials. *Nat. Photon.* **1**, 224–227 (2007).
30. Li, J. & Pendry, J. B. Hiding under the carpet: a new strategy for cloaking. *Phys. Rev. Lett.* **101**, 203901 (2008).
31. Liu, R. et al. Broadband ground-plane cloak. *Science* **323**, 366–369 (2009).
32. Gabrielli, L. H., Cardenas, J., Poitras, C. B. & Lipson, M. Silicon nanostructure cloak operating at optical frequencies. *Nat. Photon.* **3**, 461–463 (2009).

33. Valentine, J., Li, J., Zentgraf, T., Bartal, G. & Zhang, X. An optical cloak made of dielectrics. *Nat. Mater.* **8**, 568–571 (2009).
34. Chen, H. et al. Ray-optics cloaking devices for large objects in incoherent natural light. *Nat. Commun.* **4**, 2652 (2013).
35. Zheng, B. et al. 3D Visible-light invisibility cloak. *Adv. Sci.* **5**, 1800056 (2018).
36. Lai, Y. et al. Illusion optics: the optical transformation of an object into another object. *Phys. Rev. Lett.* **102**, 253902 (2009).
37. Greenleaf, A., Kurylev, Y., Lassas, M. & Uhlmann, G. Electromagnetic wormholes and virtual magnetic monopoles from metamaterials. *Phys. Rev. Lett.* **99**, 183901 (2007).
38. Narimanov, E. E. & Kildishev, A. V. Optical black hole: broadband omnidirectional light absorber. *Appl. Phys. Lett.* **95**, 041106 (2009).
39. Genov, D. A., Zhang, S. & Zhang, X. Mimicking celestial mechanics in metamaterials. *Nat. Phys.* **5**, 687–692 (2009).
40. Smolyaninov, I. I. & Narimanov, E. E. Metric signature transitions in optical metamaterials. *Phys. Rev. Lett.* **105**, 067402 (2010).
41. Cheng, Q., Cui, T. J., Jiang, W. X. & Cai, B. G. An omnidirectional electromagnetic absorber made of metamaterials. *New J. Phys.* **12**, 063006 (2010).
42. Sheng, C., Liu, H., Wang, Y., Zhu, S. N. & Genov, D. A. Trapping light by mimicking gravitational lensing. *Nat. Photon.* **7**, 902–906 (2013).
43. Danner, A. J., Tyc, T. & Leonhardt, U. Controlling birefringence in dielectrics. *Nat. Photon.* **5**, 357–359 (2011).
44. Xu, L. & Chen, H. Conformal transformation optics. *Nat. Photon.* **9**, 15–23 (2015).
45. Pendry, J. B., Luo, Y. & Zhao, R. Transforming the optical landscape. *Science* **348**, 521–524 (2015).
46. Heiblum, M. & Harris, J. H. Analysis of curved optical-waveguides by conformal transformation. *IEEE J. Quantum Electron.* **QE11**, 75–83 (1975).
47. Frateschi, N. C. & Levi, A. F. J. Resonant modes and laser spectrum of microdisk lasers. *Appl. Phys. Lett.* **66**, 2932–2934 (1995).
48. Lenz, G., Talanina, I. & de Sterke, C. M. Bloch oscillations in an array of curved optical waveguides. *Phys. Rev. Lett.* **83**, 963–966 (1999).
49. Luo, Y., Lei, D. Y., Maier, S. A. & Pendry, J. B. Broadband light harvesting nanostructures robust to edge bluntness. *Phys. Rev. Lett.* **108**, 023901 (2012).
50. Wan, X., Shen, X., Luo, Y. & Cui, T. J. Planar bifunctional Luneburg-fisheye lens made of an anisotropic metasurface. *Laser Photon. Rev.* **8**, 757–765 (2014).
51. Wang, X. et al. Self-focusing and the Talbot effect in conformal transformation optics. *Phys. Rev. Lett.* **119**, 033902 (2017).
52. Zelmon, D. E., Small, D. L. & Jundt, D. Infrared corrected Sellmeier coefficients for congruently grown lithium niobate and 5 mol.% magnesium oxide–doped lithium niobate. *J. Opt. Soc. Am. B* **14**, 3319–3322 (1997).
53. Wang, C. et al. Ultrahigh-efficiency wavelength conversion in nanophotonic periodically poled lithium niobate waveguides. *Optica* **5**, 1438–1441 (2018).
54. Yuan, S. et al. Strongly enhanced second harmonic generation in a thin film lithium niobate heterostructure cavity. *Phys. Rev. Lett.* **127**, 153901 (2021).

Publisher's note Springer Nature remains neutral with regard to jurisdictional claims in published maps and institutional affiliations.

Springer Nature or its licensor (e.g. a society or other partner) holds exclusive rights to this article under a publishing agreement with the author(s) or other rightsholder(s); author self-archiving of the accepted manuscript version of this article is solely governed by the terms of such publishing agreement and applicable law.

© The Author(s), under exclusive licence to Springer Nature Limited 2024

Methods

Theoretical methods

We propose a novel conformal mapping approach to obtain the equivalent straight waveguide from a LNOI-CAW with varying radii. We substitute the transformed permittivity and permeability into COMSOL Multiphysics (v.5.3)[55] to calculate the properties of CAWs, including effective mode index and mode area. Based on transformed wave function and transformed eigenmode field, we establish the nonlinear CWEs model in CAWs with varying indexes. We also numerically solved out the SFG intensity for different accelerations under the same initial conditions.

Sample design and fabrication

We fabricated CAWs on LNOI with varying radii as, expressed in equation (2). All CAWs were defined with an initial radius of $r(0) = 60$ μm and ended with $r(L) = 50, 40, 30, 25, 22, 20, 18, 17, 16, 15, 14$μm, with a fixed propagating length of $L = 60$ μm. The fabrication process was performed using a commercially available *z*-cut LNOI wafer (NANOLN, Jinan Jingzheng Electronics). The top lithium niobate film had a thickness of 370 nm, and was bonded to a 2 μm silica buffer, which was deposited on a 500 μm lithium niobate substrate. We mainly used electron-beam lithography for the etching process. After the CAWs were fabricated, a 50-nm-thick silver film was sputtered onto the LNOI wafer using magnetron sputtering. The couple-in and couple-out gratings were then drilled using a FIB (FEI Dual Beam HELIOS NANOLAB 600i, 30 keV, 80 pA). Finally the samples were immersed in dilute nitric acid to remove the silver film. Detailed photographs of the sample were taken by FIB and are shown in Supplementary Fig. 6. The magnification was 1,200× in the blue box, 1,500× in the orange box and 2,000× in the green box. The inset given in the red box displays the longitudinal cross section of one waveguide.

Experimental set-up and data analysis

We designed an experimental set-up (see Fig. 3a) to measure fixed-frequency and broadband SFG-ISU. We combined a tunable femtosecond laser (Spectra-physics, Mai Tai HP) and a fixed continuous-wave laser using a beam splitter, and focused them onto the sample through a microscope objective (Olympus Plan Achromat Objective 20×/0.4). The polarization was controlled by a half-wave plate. We obtained the fixed-frequency SFG enhancement directly from the images captured by the sCMOS camera (Hamamatsu, ORCA-Flash 4.0, C11440-42U). We used a spectrometer (PYLON, Princeton) and sCMOS camera to quantify the transmission of λ_{SF3} by SFG for bandwidth broadening; set the fundamental waves as $\lambda_j = 2\lambda_{SF3}$). We then normalized the SFG spectrum recorded by the spectrometer for different λ_{FF1}, and obtain the bandwidth of each CAW.

Data availability

The data that support the plots of this study are available. Any additional data are available from the corresponding author on reasonable request. Source Data are provided with this paper.

Code availability

The codes that support the findings of this study are available from the corresponding authors on reasonable request.

References

55. COMSOL Multiphysics v.5.3 (COMSOL AB, 2017).

Acknowledgements

This work was financially supported by the National Natural Science Foundation of China (grant nos. 92150302 and 92163216 to H. L., 62288101 to S. Z. and 12174187 to C.S.) and the National Key R&D Program of China (grant no. 2023YFB2805700 to C.S.). This work was sponsored by the National Research Foundation Singapore Competitive Research Program (grant nos. NRF-CRP22-2019-0006 and NRF-CRP23-2019-0007 to Y. L.), and A*STAR AME Programmatic Funds (grant no. A18A7b0058 to Y.L.).

Author contributions

H.L. and Y.L. conceived the idea. Y.L. performed the theoretical derivation. C.H. conceived the calculation, analysed the data and designed the sample. Z.Y and Y.Z fabricated the sample. H.L. and Y.Z. designed the experiments. C.H., Y.Z., X.M. and Z.L. performed the experiments. C.H., Y.L. and H.L. wrote the manuscript. All authors discussed the results. H.L. and Y.L. supervised the study.

Competing interests

The authors declare no competing interests.

Additional information

Supplementary information The online version contains supplementary material available at https://doi.org/10.1038/s41566-024-01386-2.

Correspondence and requests for materials should be addressed to Yu Luo or Hui Liu.

Peer review information *Nature Photonics* thanks the anonymous reviewers for their contribution to the peer review of this work.

Reprints and permissions information is available at www.nature.com/reprints.